

# Probing Solute–Solvent Interactions of Transition Metal Complexes Using L-Edge Absorption Spectroscopy

Raphael M. Jay,\* Vinícius Vaz da Cruz,\* Sebastian Eckert, Mattis Fondell, Rolf Mitzner, and Alexander Föhlisch

Cite This: *J. Phys. Chem. B* 2020, 124, 5636–5645

Read Online

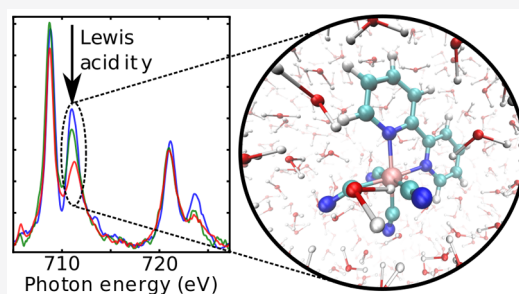
ACCESS |

Metrics & More

Article Recommendations

Supporting Information

**ABSTRACT:** In order to tailor solution-phase chemical reactions involving transition metal complexes, it is critical to understand how their valence electronic charge distributions are affected by the solution environment. Here, solute–solvent interactions of a solvatochromic mixed-ligand iron complex were investigated using X-ray absorption spectroscopy at the transition metal  $L_{2,3}$ -edge. Due to the selectivity of the corresponding core excitations to the iron 3d orbitals, the method grants direct access to the valence electronic structure around the iron center and its response to interactions with the solvent environment. A linear increase of the total  $L_{2,3}$ -edge absorption cross section as a function of the solvent Lewis acidity is revealed. The effect is caused by relative changes in different metal–ligand-bonding channels, which



preserve local charge densities while increasing the density of unoccupied states around the iron center. These conclusions are corroborated by a combination of molecular dynamics and spectrum simulations based on time-dependent density functional theory. The simulations reproduce the spectral trends observed in the X-ray but also optical absorption experiments. Our results underscore the importance of solute–solvent interactions when aiming for an accurate description of the valence electronic structure of solvated transition metal complexes and demonstrate how  $L_{2,3}$ -edge absorption spectroscopy can aid in understanding the impact of the solution environment on intramolecular covalency and the electronic charge distribution.

## INTRODUCTION

Rationalizing electronic charge distributions of transition metal (TM) complexes is a fundamental challenge in order to tailor their properties to applications in catalysis<sup>1</sup> and sustainable energy research.<sup>2</sup> This is particularly the case for the liquid phase, where a fluctuating solvent network can critically determine (photo-) chemical reactivity. In this context, it is crucial to understand how intermolecular interactions with the solvent reshape the electronic charge distribution of the solute and thus determine its catalytic capabilities. On an intramolecular level, the valence electronic structure of TM complexes is generally described by relative contributions of donation and backdonation channels that constitute the metal–ligand bond. These covalent mechanisms in turn shape the total electronic charge distribution and can be expected to be impacted by varying intermolecular interactions with a solvent. Such effects resulting from solvation are known to, for example, mediate electron transfer<sup>3,4</sup> and can govern photochemical properties on a quantitative<sup>5,6</sup> as well as qualitative level.<sup>7–9</sup>

To study the impact of solvation on the electronic structure of TM complexes on a fundamental level, iron (Fe) cyanides are well-suited model systems, since their electronic structure has been thoroughly investigated.<sup>10–13</sup> In a study on solvent effects, Penfold et al. performed  $K\alpha$  resonant inelastic X-ray

scattering (RIXS) experiments and used molecular dynamics (MD) simulations to qualitatively interpret the spectroscopic features for different solvents.<sup>14</sup> Similarly, Ross et al. employed various spectroscopies across a wide range of energies from the infrared to the X-ray regime. The study highlighted the importance of explicitly treating the solvent in quantum chemical simulations in order to ensure an accurate modeling of the electronic structure of iron cyanides.<sup>15</sup> Both studies particularly found a strong hydrogen-bonding interaction between protic solvents and the cyanide ( $\text{CN}^-$ ) ligands, which impacts intramolecular covalency. More specifically, the hydrogen bond has been reported to withdraw charge from the  $\text{CN}^-$  ligands, which is compensated for by a concomitant increase in  $\pi$ -backdonation.<sup>14</sup> This mechanism has also been used to explain the solvatochromism of mixed-ligand Fe complexes involving cyanide ligands<sup>16,17</sup> as well as their solvent-dependent photochemical pathways.<sup>8,9,18</sup>

Received: January 23, 2020

Revised: June 12, 2020

Published: June 12, 2020



In order to study such trends in the covalency of TM complexes, X-ray absorption spectroscopy<sup>19</sup> (XAS) at the TM L<sub>2,3</sub>-edge provides the most direct access to the relevant frontier orbitals. For third-row TM complexes, the underlying metal 2p → 3d excitations probe the unoccupied metal 3d orbitals.<sup>20,21</sup> Thereby, their composition and thus role in covalent metal–ligand interactions can be directly evaluated. In terms of sensitivity to the solvent, however, L<sub>2,3</sub>-edge absorption spectroscopy is rather underexplored, and experimental studies are scarce. Bonhommeau et al. studied how Fe(II) and Fe(III) ions form complexes with different alcohols, thereby deducing a polarity-dependence of the covalent solute–solvent interactions.<sup>22</sup> Hua et al. on the other hand performed a theoretical study targeting the solvation of Fe polypyridyl complexes in acetonitrile<sup>23</sup> and compared their simulations to previously published data.<sup>24,25</sup> Explicit solute–solvent interactions were found to be minimal, and the subsequent analysis was focused on structural effects.

In this work, we use XAS at the Fe L<sub>2,3</sub>-edge to study the impact of solute–solvent interactions on the valence electronic structure of the mixed-ligand Fe(II) complex [Fe(bpy)(CN)<sub>4</sub>]<sup>2-</sup> (bpy = 2,2'-bipyridine). The experiment is performed using a transmission flatjet endstation<sup>26</sup> that allows absolute X-ray absorption cross sections to be measured<sup>27</sup> for different solvents without the need to invoke edge jump normalizations as in yield-based approaches.<sup>11,20,28–30</sup> Solvent-dependent changes in π-backdonation are revealed as well as compensating donation effects that maintain local charge densities at the Fe center. These conclusions are confirmed by a combination of MD and time-dependent density functional theory (TD-DFT) that allow the observed spectroscopic trends to be reproduced. The study demonstrates a non-negligible interaction between CN<sup>-</sup>-containing TM complexes and the solvent that must be considered in future L<sub>2,3</sub>-edge spectrum simulations of metal cyanides in order to accurately describe the underlying valence electronic structure. Furthermore, the combination of MD and TD-DFT simulations can be established as an approach that reasonably accounts for the relevant interactions between closed-shell TM complexes and their solution environment.

## METHODS

**Chemicals and Materials.** K<sub>2</sub>[Fe(bpy)(CN)<sub>4</sub>]·3H<sub>2</sub>O was purchased from HetCat and directly dissolved in deionized water for the measurement in aqueous solution. To dissolve the complex in ethanol (EtOH) and dimethyl sulfoxide (DMSO), the K<sup>+</sup> counterions of the initial sample were exchanged with [N(C<sub>4</sub>H<sub>9</sub>)<sub>4</sub>]<sup>+</sup> following the procedures by Schilt<sup>31</sup> and Takasugi.<sup>16</sup> In short, the K<sup>+</sup> ions were first exchanged with H<sup>+</sup> by adding an excess of hydrochloric acid to a cooled solution of aqueous K<sub>2</sub>[Fe(bpy)(CN)<sub>4</sub>]·3H<sub>2</sub>O. The precipitated H<sub>2</sub>[Fe(bpy)(CN)<sub>4</sub>] was then filtered, washed, dried, and reacted with 2·[N(C<sub>4</sub>H<sub>9</sub>)<sub>4</sub>]OH in methanol. Finally, the solvent was evaporated under low pressure, and the product of the ion exchange was dissolved in DMSO and EtOH.

**Experimental Details.** The X-ray absorption data were measured at the UE52-SGM beamline<sup>32</sup> of the BESSY II light source using a transmission flatjet system described by Fondell et al.<sup>26</sup> Complementary measurements have been performed at the EDAX@UE49-SGM experiment. The sample is delivered into the experimental chamber by two colliding round jets with a diameter of about 30 μm. Thereby, a free-flowing liquid leaf

is formed under vacuum conditions.<sup>33</sup> The leaf exhibits a thickness of several μm, which allows for the transmission of X-rays at 3d L<sub>2,3</sub>-edges,<sup>27</sup> while the constant sample replenishment prevents potential X-ray-induced sample damage.<sup>34</sup> Depending on the solvent, different flow rates are required to keep the jet stable. The flow rate was 2.0 mL/min for water, 1.3 mL/min for EtOH, and 1.6 mL/min for DMSO. The intensity transmitted through the sample was detected as the average current of a gallium arsenide photodiode and recorded as a function of the X-ray photon energy. The bandwidth of the incident X-ray radiation was 0.3 meV at 700 eV of excitation energy. Details on experimental procedures and data treatment can be found in the [Supporting Information](#).

**Computational Details.** All molecular dynamics simulations were carried out with the Gromacs2019 package.<sup>35</sup> The SPC/F<sub>w</sub><sup>36</sup> force-field (FF) was adopted for the simulations in water, while the OPLS-aa<sup>37</sup> FF was used for EtOH and DMSO. The parameters describing intermolecular interactions for the K<sup>+</sup> counterions were taken from ref 38. To describe the bonded interactions of the solute, a specific parametrization was carried out via the JOYCE procedure.<sup>39</sup> The fitting was based on the optimized structure and the Hessian of the complex in the gas phase, which were obtained at the DFT/B3LYP<sup>40,41</sup> level with the def2-TZVP(-f)<sup>42</sup> basis set, employing the D3BJ dispersion correction.<sup>43,44</sup> The RIJCOSX<sup>45</sup> approximation was used with the def2-TZV/J auxiliary basis set<sup>46</sup> as implemented in the ORCA quantum chemistry package.<sup>47</sup> To describe the nonbonded interactions, the Lennard-Jones parameters for Fe were transferred from ref 48, while for C and N, the parameters from ref 49 were adopted (analogously to ref 50). For the Coulomb interaction term, point charges were derived using the CHELPG<sup>51</sup> fitting procedure in the Multiwfn<sup>52</sup> program. See the [Supporting Information](#) for the full set of parameters used in the MD simulations along with additional details.

The spectra in the liquid phase were calculated as the sum of spectra from 50 uncorrelated snapshots taken from the MD simulations, however, with a reduced number of explicit solvent molecules. The details of the solvation model adopted for each solvent will be given further in the text. In addition, the bulk solvation effects were accounted for implicitly via the conductor-like polarizable continuum model (CPCM).<sup>53</sup> The spectra for each snapshot were computed with linear response TD-DFT. For the optical excitations, the lowest 50 singlet states were computed. The core-level spectra were obtained by restricting the excitation orbital window to include only the Fe 2p orbitals, and then, 100 singlet and 100 triplet core-states were computed. Finally, the spin–orbit coupling was taken into account perturbatively via the mean-field spin–orbit operator as described in ref 54. All spectrum calculations utilized the hybrid M06<sup>55</sup> exchange and correlation functional, which was benchmarked to best reproduce the optical MLCT band as well as L<sub>2,3</sub>-edge spectra. A more detailed discussion on functional choice and a comparison with other popular functionals is shown in the [Supporting Information](#).

In order to disentangle the orbital contributions to the metal–ligand bond, a fragment decomposition of the molecular orbitals of the system was carried out using the charge decomposition analysis scheme<sup>56,57</sup> (CDA). To minimize nonphysical populations (due to the Mulliken partition), the smaller, closely related def2-SV(P) basis set was employed for the decomposition. This analysis was carried

out with the Multiwfn program.<sup>52</sup> Details regarding the analyzed orbitals can be found in the Supporting Information.

## RESULTS AND DISCUSSION

Figure 1a shows the molecular structure of  $[\text{Fe}(\text{bpy})(\text{CN})_4]^{2-}$ . The complex is coordinated with four  $\text{CN}^-$  and one 2,2'-

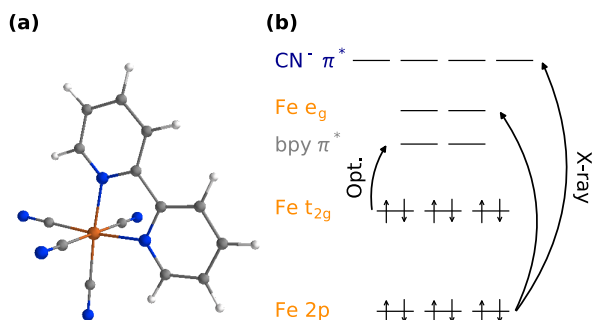


**Figure 1.** (a) Gas-phase molecular structure and (b) valence electronic structure of  $[\text{Fe}(\text{bpy})(\text{CN})_4]^{2-}$  as well as a schematic single-electron representation of the optical and X-ray absorption processes.

bipyridine (bpy) group, which allows the complex to be approximated as octahedral and its properties to be discussed within the notation of the  $O_h$  point group. The corresponding valence electronic structure is shown in Figure 1b in terms of a molecular orbital diagram.  $[\text{Fe}(\text{bpy})(\text{CN})_4]^{2-}$  can be described as a nominal Fe(II) closed-shell singlet with the Fe-3d-derived orbitals being the fully filled  $t_{2g}$ - and completely unoccupied  $e_g$ -orbitals. The complex furthermore exhibits unoccupied ligand  $\pi^*$ -orbitals from the bpy as well as  $\text{CN}^-$  groups. Due to the underlying selection rules and as indicated in the scheme, the different unoccupied ligand  $\pi^*$ -orbitals can be independently accessed by either optical or X-ray absorption spectroscopy. Here, the two experimental techniques therefore serve as complementary probes of the valence electronic structure.

The optical absorption spectra of  $[\text{Fe}(\text{bpy})(\text{CN})_4]^{2-}$  dissolved in water, EtOH, and DMSO are displayed in Figure 2a. The two bands can be attributed to Fe  $t_{2g} \rightarrow \text{bpy} \pi^*$ -metal-to-ligand charge-transfer (MLCT) excitations, whose energies shift as a function of the solvent. The MLCT energies have been shown to scale linearly with the acceptor number (AN),<sup>16</sup> which constitutes an empirical measure of the solvent Lewis acidity. Thereby, the AN accounts for both nonspecific interactions like the solvent polarizability as well as the hydrogen bond donation ability.<sup>58</sup> Within this framework, the solvatochromic behavior of the complex has been rationalized by negative charge being withdrawn (accepted) by the solvent from the  $\text{CN}^-$  ligands via nonspecific interactions as well as hydrogen-bonding (depending on the solvent). The resulting charge deficiency is compensated for by an increase in  $\pi$ -backdonation from the metal center onto the  $\text{CN}^-$  ligands. This stabilizes the  $t_{2g}$ -orbitals and subsequently linearly increases MLCT excitation energies with higher Lewis acidity.<sup>16</sup> Due to their sensitivity to intramolecular bonds, a similar linearity for metal–cyanide complexes has been revealed by IR spectroscopy.<sup>17</sup>

The complementary transmission X-ray absorption measurements at the Fe  $L_{2,3}$ -edge are displayed in Figure 2b for  $[\text{Fe}(\text{bpy})(\text{CN})_4]^{2-}$  in the same three solvents. The recorded

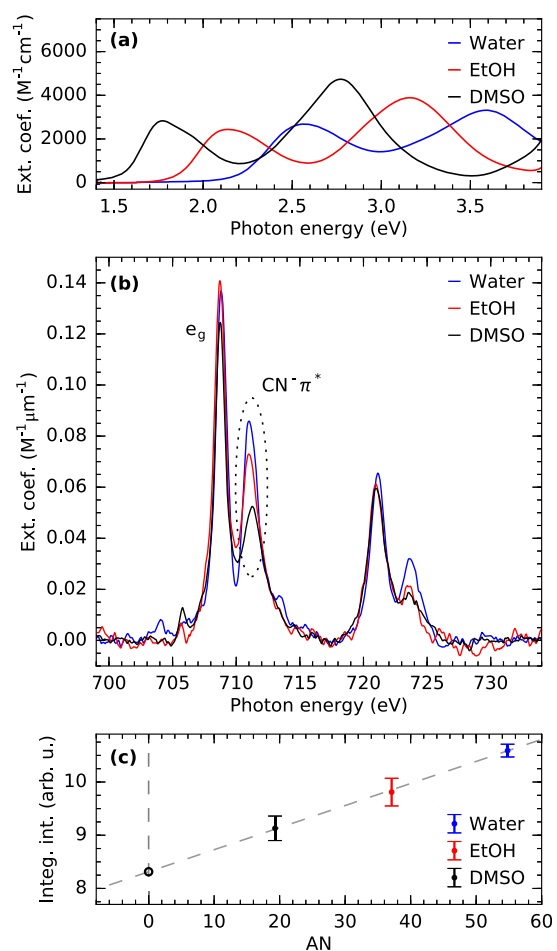


**Figure 2.** (a) Optical absorption spectra of  $[\text{Fe}(\text{bpy})(\text{CN})_4]^{2-}$  in water, EtOH, and DMSO exhibiting the previously reported solvent-dependent shift of the MLCT bands. (b) Fe  $L_{2,3}$ -edge X-ray absorption spectra of  $[\text{Fe}(\text{bpy})(\text{CN})_4]^{2-}$  in water, EtOH, and DMSO measured with a transmission flatjet. The decrease of the Fe  $2p \rightarrow \text{CN}^- 2\pi^*$ -transition is a signature of reduced  $\pi$ -backdonation in solvents with low Lewis acidity. (c) Integrated intensities of the spectra in (b) across the full spectral range, yielding a linear-dependence of the solvent AN.

signals are background-corrected for solvent absorption by a linear fit of the pre-edge region ( $E_{\text{photon}} < 703$  eV) as well as continuum excitations from  $2p_{3/2}$  and  $2p_{1/2}$  core holes by two arctangent functions following procedures by Wasinger et al.<sup>20</sup> and Cho et al.<sup>25</sup> Each spectrum is then normalized to the sample concentration and the thickness of the respective liquid leaf (deduced from the absorption at 700 eV in comparison to tabulated values<sup>59</sup>). In analogy to optical absorption spectroscopy, this yields the extinction coefficient as the final entity independent of experimental parameters. In contrast to the optical regime, however, the extinction coefficient in this case is displayed in the unit of  $\text{M}^{-1} \mu\text{m}^{-1}$  corresponding to typical attenuation lengths in the soft X-ray regime.

The general shape of all three X-ray absorption spectra is very similar to previous partial fluorescence yield measurements of aqueous  $[\text{Fe}(\text{bpy})(\text{CN})_4]^{2-}$  by the authors.<sup>60</sup> There, the two main transitions at the  $L_3$ -edge could be assigned to be of predominantly Fe  $2p \rightarrow e_g$  (708.7 eV) and Fe  $2p \rightarrow \text{CN}^- \pi^*$  (711 eV) excitation character. When comparing the three spectra presented here, the former resonance appears to be rather insensitive to the solvent environment, and the visible

differences are well within the margin of error resulting from the normalization procedure and background subtraction (see Supporting Information). This is consistent with the Fe-centric character of the  $2p \rightarrow e_g$ -excitation. In contrast, substantial differences can be observed at the  $Fe\ 2p \rightarrow CN^- \pi^*$ -excitation. The underlying transition effectively probes the Fe 3d character of the  $CN^- \pi^*$ -system locally at the metal center. Consequently, the feature has previously been identified as a “direct probe of back-bonding”.<sup>11</sup> The measurements clearly show an increasing peak height in solvents with higher Lewis acidity (in the direction of DMSO, EtOH, water). This spectral trend therefore provides direct evidence for the previously reported enhancement of  $\pi$ -backdonation by strong Lewis acids in agreement with the results from optical and IR spectroscopy.<sup>16,17</sup>

As mentioned before, these studies additionally established linear trends between their spectroscopic observables and the solvent Lewis acidity. Figure 2c therefore shows the integrated  $L_{2,3}$ -edge intensity over the measured spectral range. It can be seen that the resulting total X-ray absorption cross section exhibits a similar dependence to the solvent Lewis acidity. The total  $L_{2,3}$ -edge absorption decreases linearly once the Lewis acidity (corresponding ANs taken from ref 58) of the solvent is reduced. When extrapolating this trend, one can acquire the corresponding cross section for the gas-phase complex or within a noninteracting solvent (e.g., hexane).  $L_{2,3}$ -edge absorption cross sections have been shown to scale with the number of nominally unoccupied d orbitals as well as the covalency of the complex.<sup>11,20,27</sup> As we compare an Fe(II) complex with unchanged 3d occupation within different solvents, the linear increase of the absorption cross section can therefore be expected to directly reflect changes in covalency as a function of the solvent Lewis acidity.

To substantiate these interpretations, we performed MD simulations to, in a first step, acquire information on the structural arrangements of  $[Fe(bpy)(CN)_4]^{2-}$  within the three different solvents. The main results of these simulations in terms of solvation structures are presented in Figure 3. Due to the mixed-ligand character of  $[Fe(bpy)(CN)_4]^{2-}$ , the solvation of the complex exhibits varying degrees of asymmetry in the

different solvents. Figure 3a shows the pair correlation functions between the N sites of the  $CN^-$  groups with the H and O atoms of water and EtOH. In the case of DMSO, pair correlation functions between the  $CN^-$  N sites and the S and O atoms are shown. In the case of the two protic solvents, the hydrogen-bonding causes a pronounced solvation shell with the first maxima being located at N–H bond distances of 1.7 and 1.8 Å in water and EtOH, respectively. Due to the absence of hydrogen-bonding in the case of DMSO, the coordination is significantly less structured at largely increased average solute–solvent bond distances.

A closer look at the hydrogen-bonding properties of the complex reveals that, on average, the cyanide ligands experience  $2.5 \pm 0.4$  hydrogen bonds in water and  $1.8 \pm 0.4$  hydrogen bonds in ethanol (number of hydrogen bonds defined for  $r_{N-O} < 3$  Å and  $\angle NHO < 20^\circ$ ). It should also be noted that there are some inhomogeneities in the solvation shell of the cyanides with the axial ligands displaying a slightly higher average number of hydrogen bonds than the ones lying in the bpy plane, (The full analysis is available in the Supporting Information.)

A different picture, however, is given from the perspective of the bpy group. Figure 3b shows the pair correlation functions between the H atoms of the bpy group and O and H atoms of the two protic solvents. For the case of DMSO, pair correlation functions between the bpy H atoms and the O and S atoms are shown. Judging from the comparably unstructured coordination in all three solvents, solute–solvent interactions between the bpy group and the two protic solvents seem to be much smaller than at the  $CN^-$  side, while a similarly small interaction is observed for the case of DMSO. In order to build a realistic but manageable solvation model for the simulation of the experimental spectra, it therefore seems reasonable to make the following approximations. For the case of water and EtOH, molecules of the first solvation shell around the  $CN^-$  ligands are explicitly included. The bulk solvent beyond that as well as the molecules coordinating with the bpy group are modeled implicitly by a CPCM approach. Due to the absence of coordinated solute–solvent interactions between  $[Fe(bpy)(CN)_4]^{2-}$  and DMSO, we only consider the structural evolution of  $[Fe(bpy)(CN)_4]^{2-}$  in DMSO but model the solvent solely with a CPCM approach.

The results of the simulations for the optical regime are presented in Figure 4. There, the previously introduced experimental absorption spectra in the three different solvents (a) are compared to the spectrum simulations (b). All simulated spectra represent an average of over 50 TD-DFT calculations on uncorrelated snapshots of our MD simulations with the structures being reduced as previously described. Each calculated transition is convoluted with a 0.2 eV Gaussian function to account for an estimated broadening due to vibronic contributions as well as an undersampling by the used 50 snapshots. Due to the comparably long lifetime of the valence-excited final states, a Lorentzian broadening is neglected. The calculated spectrum in water is normalized to the maximum of the low-energy MLCT band in the experimental spectrum and shifted by 0.4 eV. The calculated spectra for EtOH and DMSO are scaled and shifted accordingly. When comparing the experimental and theoretical optical absorption spectra in Figure 4a,b, the model fully reproduces the experimentally observed shift in energy of the two MLCT bands with only a slight underestimation of the shift for the case of DMSO. Our simulations further confirm

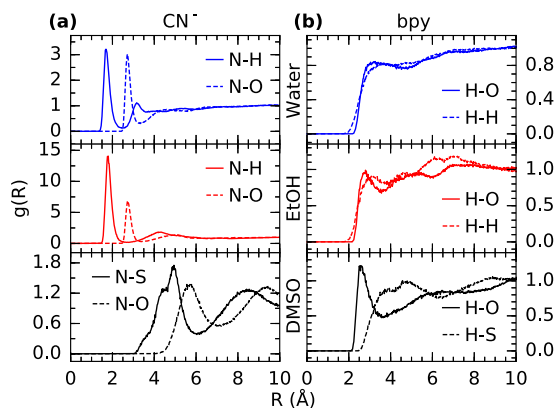


**Figure 3.** (a) N–H and N–O pair correlation functions between the  $CN^-$  groups and the solvent for water (top) and EtOH (middle) as well as N–S and N–O pair correlation functions for DMSO (bottom). (b) H–O and H–H pair correlation functions between the bpy group and the solvents for water (top) and EtOH (middle) as well as H–O and H–S pair correlation functions for DMSO (bottom).

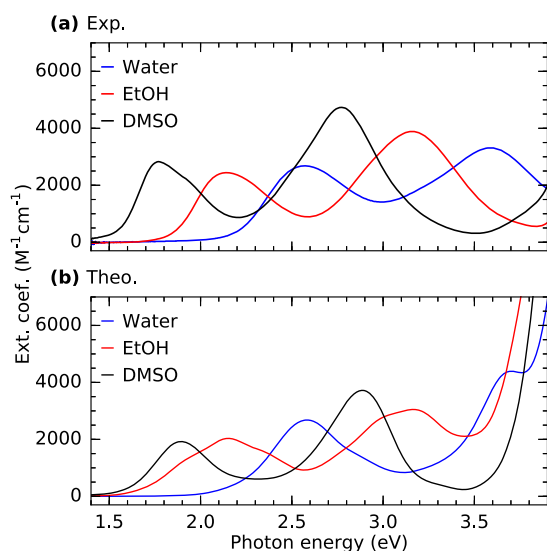


**Figure 4.** (a) Optical absorption spectra of  $[\text{Fe}(\text{bpy})(\text{CN})_4]^{2-}$  in water, EtOH, and DMSO compared to (b) simulated spectra based on sampled TD-DFT calculations reproducing the experimentally observed shift of the MLCT bands.

previous notions<sup>8,9,16</sup> that this shift is caused by, on average, lower  $t_{2g}$ -orbital energies in water than in EtOH and DMSO. These findings as well as the agreement with the experimental spectra thus allow it to be concluded that the applied model represents a reasonable description of the solute–solvent interactions in the three different solvents. It should further be emphasized that it is crucial to explicitly include water and EtOH molecules, since neglecting the associated hydrogen-bonding does not allow the experimentally observed spectral shifts to be reproduced (see Supporting Information).

We therefore proceed to the X-ray regime, where the results of the simulations are presented in Figure 5. Analogously to the optical spectra, the simulations are based on 50 TD-DFT snapshots. It should be noted that TD-DFT cannot be expected to fully account for 3d–3d and 2p–3d correlation effects in the core-excited final state of the  $L_{2,3}$ -edge absorption process. However, the approach has successfully been implemented previously to model the  $L_3$ -edge absorption spectra of closed-shell Ru<sup>61,62</sup> as well as Fe complexes.<sup>23</sup>

Similarly to the optical absorption spectra, all calculated X-ray transitions in Figure 5b are convoluted with an experimental Gaussian broadening of 0.3 eV as determined from the beamline bandwidth at a photon energy of 700 eV. An additional broadening of 0.2 eV is deduced by comparison to the calculations by Hua et al.,<sup>23</sup> which accounts for vibronic contributions to the spectra. Furthermore, a broadening of 0.5 eV is estimated to again account for the supposed under-sampling. Lastly, a 0.4 eV Lorentzian broadening is applied to account for the lifetime of the 2p core hole.<sup>63</sup> All calculated spectra are shifted by 10.3 eV to match the experimental spectra. It is important to note that in analogy to the absolute absorption cross sections measured in the experiment, each simulated spectrum for the three different solvents is displayed based on absolute oscillator strengths, which are only normalized to the number of snapshots and broadened according to the previously described procedure. Thereby, the very similar intensities of the  $e_g$ -resonance at 708.7 eV are reproduced. This verifies the experimentally deduced insensitivity of its metal-centric character to the solvent environment. This comparability, however, does not necessarily hold for the spectrum of the optimized gas-phase structure, which is additionally shown. Due to the absence of intermolecular interactions in the gas-phase, the applied broadening (which is the same as for the spectra of the solvated complex) overestimates the structural variations of an isolated molecule, which are expected to be lower than in the case of a solvated molecule. For comparability, the gas-phase spectrum is therefore scaled to the maximum of the sampled spectrum in water.

When comparing the four simulated X-ray absorption spectra, a decrease of the second resonance can be observed in the series of decreasing Lewis acidities from water to the gas-phase, however, with DMSO as an outlier. We attribute this to the insufficient treatment of our solvation model, where in contrast to the optical absorption, the modeling with a CPCM approach seems to not fully account for the solute–solvent interaction. We expect a full explicit treatment of DMSO molecules of the first solvation shell around the  $\text{CN}^-$  as well as the bpy ligands to account for this discrepancy. When again evaluating the correlation functions of DMSO displayed in Figure 3, the coordination structure around the ligands, though significantly smaller than in the two protic solvents,

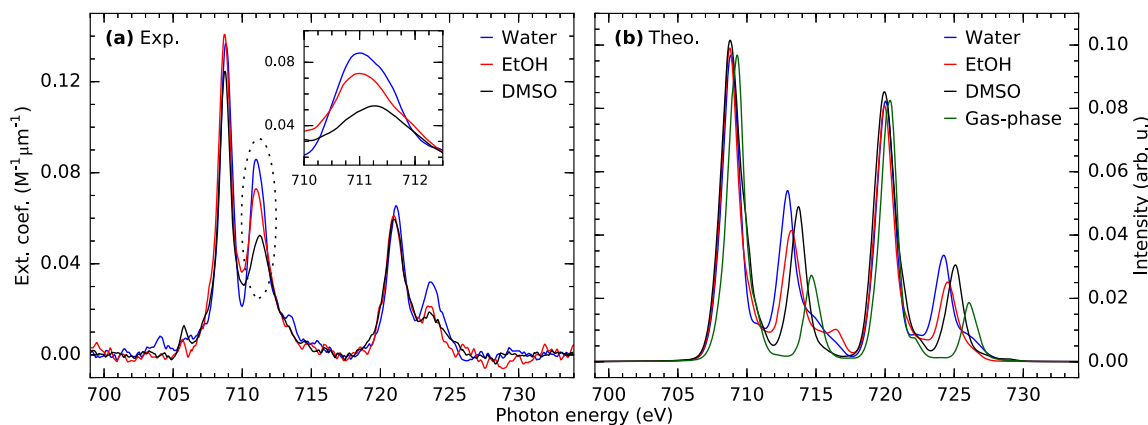


**Figure 5.** (a) Measured solvent-dependent Fe  $L_{2,3}$ -edge X-ray absorption spectra of  $[\text{Fe}(\text{bpy})(\text{CN})_4]^{2-}$  compared to (b) simulated spectra based on sampled TD-DFT calculations as well as a single-structure calculation of the gas-phase molecule (scaled by a factor of 0.71 to the maximum of the water spectrum).

appears to be more crucial for the description of the X-ray absorption spectra than expected. An explicit treatment of the full first solvation shell of DMSO in the simulations is, however, computationally unfeasible at the employed level of theory. Nevertheless, the failure of the model for the X-ray regime, although reproducing the optical spectra, emphasizes the particular sensitivity of  $L_{2,3}$ -edge absorption spectroscopy to the solvent environment.

Despite the discrepancies for the case of DMSO, the model reproduces the spectral trends observed for the two protic solvents and with respect to the gas phase. We therefore proceed to rationalize the underlying mechanism with the proposed solvation model as a starting point and by comparing the case of water to the gas phase. It should be noted that the solvation model is, in order to reproduce the ensemble average detected within the measurements, based on a manifold of structures. For the sake of simplicity, we therefore employ a reduced model that still captures the essential properties of the water environment. It is based on the gas-phase structure of the complex, however, embedded in an idealized solvent structure, as determined from the MD simulations. Deduced from the previously presented hydrogen bond analysis of the complex in water, this amounts to approximately three hydrogen bonds between each  $\text{CN}^-$  group and the surrounding waters with respect to the  $\text{CN}^-$  group. The positions of the water molecules were chosen to mimic the first solvation shell of the cyanides, based on bond lengths and angles from the MD simulation (see [Supporting Information](#)), however, with the additional requirement that  $C_{2v}$  symmetry was preserved, to ease the comparison to the gas-phase complex. This model therefore neglects structural differences but allows effects caused by interaction with the solvent to be isolated.

The exemplified structure is shown in [Figure 6a](#). It is displayed as a charge-density difference, where the density of the solvated structure  $\rho_{\text{sol}}$  is compared to the gas-phase charge-density  $\rho_{\text{gas}}$ . The charge density of the eight water molecules  $\rho_{\text{H}_2\text{O}}$ , which is calculated without the presence of the complex, is additionally subtracted. The displayed charge density is therefore calculated as  $\rho = \rho_{\text{sol}} - \rho_{\text{gas}} - \rho_{\text{H}_2\text{O}}$ . It can be clearly seen that the introduction of solvent molecules causes a manifold of charge redistribution effects throughout the  $\text{CN}^-$  ligands as well as the Fe center. Our qualitative analysis is, however, restricted to a single  $\text{CN}^-$  group as displayed in [Figure 6b](#), since analogous effects (however, to a smaller degree for the axial ligands) can be seen for the other  $\text{CN}^-$  ligands. In order to rationalize the observed changes also in terms of changes to the metal–ligand bond, [Table 1](#) shows a decomposition of a selected set of molecular orbitals into contributions from different molecular fragments (see [Computational Details](#) and [Supporting Information](#)). In the discussion below, metal-centered 3d orbitals are referred to as Fe 3d orbitals and ligand-centered orbitals as either  $\text{CN}^-(\pi)$ ,  $(\pi^*)$ ,  $(\sigma)$ , and  $\text{bpy}(\pi^*)$ . Approximate  $O_h$  labels are used for simplicity, instead of the strict  $C_{2v}$  notation shown in the [Supporting Information](#).

Starting from the solvent, it can be observed how the water molecules are polarized in a way that negative charge accumulates on one side and a positively charged hydrogen points toward the ligand. This allows the N site of the  $\text{CN}^-$  group to accommodate additional electronic charge within a  $\pi$ -shaped orbital similar to observations of the HCN molecule in

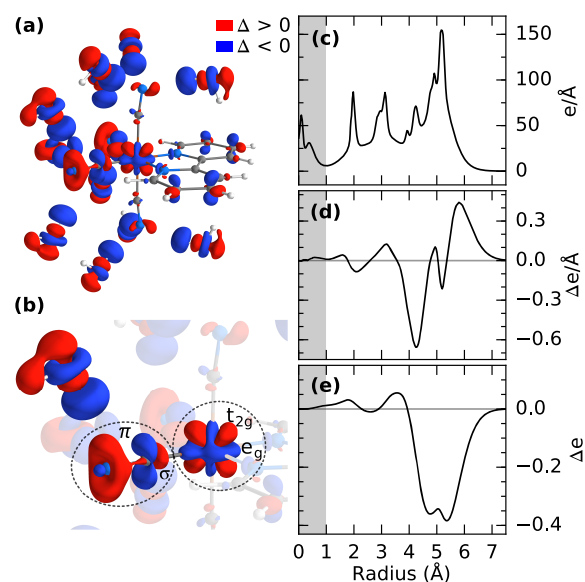


**Figure 6.** (a) Charge-density difference between the reduced solvation model and the gas-phase complex plotted at an isovalue of 0.0025. (b) Single-ligand picture yielding an increase in  $\pi$ -backdonation as well a decrease in  $\sigma$ -donation. (c) Charge density of the solvated complex as a function of the radius from the Fe center. Charge density below 1 Å corresponds to Fe charge density and is marked in gray. (d) Charge-density difference between the solvated and the gas-phase molecule as a function of the radius showing only marginal changes around the Fe center (the charge density of the water molecules is additionally subtracted). (e) Integrated charge-density difference yielding a net change in charge of about 1% at the Fe center.

**Table 1. Percentage-wise Orbital Decomposition of the Occupied Fe 3d Orbitals Yielding Changes in  $\pi$ -Backdonation and  $\pi$ -Bonding between the Gas Phase and the Reduced Solvation Model<sup>a</sup>**

|           | occ. Fe 3d     |                      |                    |                     | occ. $\text{CN}^-(\sigma)$ |
|-----------|----------------|----------------------|--------------------|---------------------|----------------------------|
|           | Fe( $t_{2g}$ ) | $\text{CN}^-(\pi^*)$ | $\text{CN}^-(\pi)$ | $\text{bpy}(\pi^*)$ | Fe( $e_g$ )                |
| gas phase | 74.4           | 4.2                  | 11.0               | 6.3                 | 10.8                       |
| solvated  | 78.4           | 5.7                  | 7.5                | 3.2                 | 5.2                        |

<sup>a</sup>Changes in  $\sigma$ -donation are presented as the Fe  $e_g$ -contribution to a set of  $\text{CN}^-$  orbitals of dominantly  $\sigma$ -character.

the presence of an electric dipole.<sup>64</sup> We interpret this as the signature of increased  $\pi$ -backdonation, as deduced from the experimental X-ray absorption spectra. This interpretation is in full agreement with the increased  $\text{CN}^-(\pi^*)$  contribution to the occupied Fe 3d orbitals (see [Table 1](#)). The fragment decomposition furthermore reveals a decrease in  $\pi$ -bonding, the mixing between occupied  $\text{CN}^-(\pi)$  and Fe 3d orbitals, which has been suggested previously.<sup>9</sup> Since this mechanism constitutes the mixture between two occupied orbitals, it does, however, not affect the overall charge distribution. Interestingly, the increase in charge density at the N site is not at the expense of the  $t_{2g}$ -character of the occupied Fe 3d orbitals, as one would intuitively expect from the backdonation process, since it is usually referred to as a delocalization of metal  $t_{2g}$ -electronic charge onto the ligand. On the contrary, an increase of  $t_{2g}$ -like charge density can be seen. This is due to a concomitant decrease of  $\pi$ -backdonation onto the bpy ligands, which can be seen in [Figure 6a](#) from the decrease in  $\pi$ -shaped charge density on the bpy ligand and is confirmed by the

fragment decomposition, which yields a reduced admixture of  $\text{bpy}(\pi^*)$  character to the occupied Fe 3d orbitals (compare Table 1). The depletion of the  $t_{2g}$ -character of the occupied Fe 3d orbitals due to the increase in  $\pi$ -backdonation onto the  $\text{CN}^-$  ligands is thereby overcompensated and results in a net increase of  $t_{2g}$ -charge density. Spectroscopically, this effect can, however, not be observed, since the corresponding core excitations into the  $\text{bpy}(\pi^*)$  orbitals are buried under the intense transitions into the metal-centric  $e_g$ -orbitals.

A loss of metal charge density can instead be found in the  $e_g$ -manifold. This can be understood as a compensating mechanism that maintains local charge densities similar to effects observed for charge-transfer excitations<sup>18,30</sup> and oxidation/reduction processes<sup>65</sup> in covalent Fe complexes. As  $\sigma$ -density additionally localizes at the C site, this compensating effect can therefore be interpreted as a reduced degree of  $\sigma$ -donation. This conclusion is again confirmed by the orbital decomposition (see Table 1), where a decrease of Fe  $e_g$ -contribution to occupied  $\text{CN}^-$  orbitals of dominantly  $\sigma$ -character can be observed. Lastly, it should be noted that additional effects such as the decrease in charge density at the C site can be observed that are most likely caused by differences in the weight of  $\pi$ - and  $\sigma$ -like contributions to the occupied  $\text{CN}^-$  orbitals as well as the significant mixing of, in particular, occupied  $\text{CN}^-(\pi)$  orbitals with water upon solvation (see Supporting Information). Additional measurements at the N K-edge<sup>64</sup> could further elucidate the effects of this behavior on the intraligand-bonding by providing the complementary ligand perspective of the underlying changes in orbital character.

In order to quantify the effect of the revealed changes in metal–ligand covalency on the overall charge distribution, Figure 6c shows the charge density of the solvated complex as a function of the radius  $R$  from the Fe center (in analogy to previous work by the authors<sup>18</sup> as well as Johansson et al.<sup>65</sup> and Kubin et al.<sup>66</sup>). At radii below 1 Å, the Fe L and M shells can be seen, while at bigger distances from the Fe center, the charge density can be attributed to the different ligands as well as the water molecules. The charge-density difference between the solvated complex and the gas-phase molecule is shown in Figure 6d. Only a marginal change can be observed in the Fe M shell in the case of the solvated complex. When integrated (compare Figure 6e), this amounts to an increase of  $\sim 1\%$  of an electronic charge at the Fe center. Changes in local metal charge are traditionally expected to be accompanied by shifts in the absorption onset of  $L_{2,3}$ -edge spectra.<sup>60,67,68</sup> An increase/decrease in negative charge would therefore lower/raise the excitation energy due to variations of the effective screening of the 2p core hole. The absence of any observable onset shift for the measurements in the three different solvents (compare Figure 5a) therefore is in agreement with the quantitative analysis of the reduced model, which revealed only a negligible change in local charge. This demonstrates how the solvent environment introduces sufficient degrees of freedom to allow for a full compensation of local charge-density variations around the Fe center. This is facilitated by the previously described charge-density rearrangements between the  $\sigma$ - and  $\pi$ -manifolds, however, to varying degrees in the different solvents. It is important to note that the constant absorption onset for the three different solvents is fully reproduced by the spectrum simulations, thereby again reinforcing the validity of the applied model underlying the spectrum calculations of the solvated complex (compare Figure

5b). The gas-phase spectrum, however, exhibits a slight shift of the absorption onset with respect to the spectra of the solvated molecule. Since the reduced model in Figure 6 yields only marginal changes in local charge at the Fe center, this is therefore more likely the result of structural effects induced by solvation. This potentially has an impact on the associated orbital energies, which in turn can affect the configuration interaction between core-excited states within the  $e_g$ -manifold.

Within this framework of charge-density compensation effects, we can finally also qualitatively rationalize the linear increase of the total absorption cross section with higher solvent Lewis acidity as shown in Figure 2c. As previously discussed, the increase in  $t_{2g}$ -like charge density can be attributed to a reduction in  $\pi$ -backdonation onto the bpy ligand. In order to compensate for this excess of negative electronic charge, a concomitant decrease in  $\sigma$ -donation can be observed, which lowers the Fe  $e_g$ -content in occupied  $\text{CN}^-(\sigma)$  orbitals and thus decreases Fe  $e_g$ -like charge density at the metal center. This could be interpreted as an effective increase of the density of unoccupied states around the metal center. Within this reasoning, the overall higher absorption cross sections for higher solvent Lewis acidity would then correspond to an increase of unoccupied states as seen through the 2p core electron. This interpretation might seem contradictory to the orbital-based interpretation of the two resonances in the  $L_{2,3}$ -edge absorption spectrum, which would consequently predict changes in the  $e_g$  in addition to the ones in the  $\text{CN}^- \pi^*$ -resonance. It should be noted, however, that the final states of the two transitions are not fully independent, resulting in limitations of the applied single-electron picture. It has been shown previously for the case of  $[\text{Fe}(\text{CN})_6]^{4-}$  that the  $\text{CN}^- \pi^*$ -resonance can “borrow” intensity from the  $e_g$ -resonance by configuration interaction in the core-excited final state, where the degree of mixing is determined by the energy separation between the two resonances.<sup>11</sup> To a small extent, this can be also observed in the experimental spectra. The  $\text{CN}^- \pi^*$ -resonance, at least for the case of DMSO, clearly exhibits a small shift to higher energies with respect to the spectrum in water (see inset in Figure 5a). This effect is also captured by our calculations, where the shifts to higher energies are however overestimated. This has been also observed in previous DFT calculations on  $[\text{Fe}(\text{bpy})(\text{CN})_4]^{2-}$  based on the restricted open-shell configuration singles method.<sup>18,69</sup> It should also be pointed out that the energy separation between the  $e_g$ - and  $\pi^*$ -resonances is quite sensitive to the amount of Hartree–Fock exchange included in the functional (see Supporting Information). Lastly, simulations based on single-determinant reference methods like TD-DFT can, however, not be expected to fully account for the underlying final state effects of the core-excited state, since even restricted active space spectrum calculations struggle to correctly reproduce the energy of the  $\text{CN}^- \pi^*$ -resonance of Fe cyanides.<sup>13,70</sup> Future ab-initio efforts<sup>13,70–73</sup> that are capable of explicitly accounting for the solvent environment will be necessary to fully rationalize the underlying mechanisms.

## CONCLUSION

In this work, we have demonstrated how  $L_{2,3}$ -edge absorption spectroscopy can be sensitive to charge rearrangements in TM complexes resulting from a varying solution environment. For the case of the mixed-ligand solvatochromic complex  $[\text{Fe}(\text{bpy})(\text{CN})_4]^{2-}$ , we have revealed an increase in  $\pi$ -backdonation as a function of the solvent Lewis acidity, which can

be directly inferred from the experimental  $L_{2,3}$ -edge absorption spectrum. Furthermore, a linear increase of the absorption cross section can be observed, which is caused by a concomitant decrease in  $\sigma$ -donation that maintains the absolute local charge densities around the Fe center.

Our findings can serve as a benchmark for generally describing the interaction of TM cyanide complexes with a solution environment and how this interaction alters the valence electronic structure to a varying degree depending on the solvent's Lewis acidity. Furthermore, the combination of MD and TD-DFT simulations could be established as a framework that is capable to qualitatively account for the dominant spectral changes in  $L_{2,3}$ -edge absorption measurements of closed-shell systems caused by solute–solvent interactions. This was achieved by explicitly considering the solvent as a part of the total molecular entity, which allowed charge rearrangements to be followed throughout the solute–solvent interface. Further theoretical developments based on multiconfigurational approaches will be necessary, however, in order to achieve a more quantitative agreement between simulation and experiment. This will further allow final state effects within the core-excited state to be fully rationalized as well as the framework to be expanded to a wider range of systems including the important class of open-shell TM complexes.

## ■ ASSOCIATED CONTENT

### Supporting Information

The Supporting Information is available free of charge at <https://pubs.acs.org/doi/10.1021/acs.jpcc.0c00638>.

Additional details on data acquisition and data treatment as well as details of the molecular dynamics simulations, hydrogen bond analysis, functional benchmarking, and charge decomposition analysis (PDF)

## ■ AUTHOR INFORMATION

### Corresponding Authors

Raphael M. Jay – Universität Potsdam, Institut für Physik und Astronomie, 14476 Potsdam, Germany; [orcid.org/0000-0001-9607-8264](https://orcid.org/0000-0001-9607-8264); Email: [rajay@uni-potsdam.de](mailto:rajay@uni-potsdam.de)

Vinicius Vaz da Cruz – Universität Potsdam, Institut für Physik und Astronomie, 14476 Potsdam, Germany; Email: [vazdacruz@uni-potsdam.de](mailto:vazdacruz@uni-potsdam.de)

### Authors

Sebastian Eckert – Universität Potsdam, Institut für Physik und Astronomie, 14476 Potsdam, Germany; [orcid.org/0000-0002-1310-0735](https://orcid.org/0000-0002-1310-0735)

Mattis Fondell – Helmholtz-Zentrum Berlin für Materialien und Energie GmbH, Institute for Methods and Instrumentation for Synchrotron Radiation Research, 12489 Berlin, Germany

Rolf Mitzner – Helmholtz-Zentrum Berlin für Materialien und Energie GmbH, Institute for Methods and Instrumentation for Synchrotron Radiation Research, 12489 Berlin, Germany

Alexander Föhlisch – Universität Potsdam, Institut für Physik und Astronomie, 14476 Potsdam, Germany; Helmholtz-Zentrum Berlin für Materialien und Energie GmbH, Institute for Methods and Instrumentation for Synchrotron Radiation Research, 12489 Berlin, Germany

Complete contact information is available at: <https://pubs.acs.org/doi/10.1021/acs.jpcc.0c00638>

## Notes

The authors declare no competing financial interest.

## ■ ACKNOWLEDGMENTS

R.M.J., V.V.C., S.E., and A.F. acknowledge funding from the ERC-ADG-2014 - Advanced Investigator Grant No. 669531 EDAX under the Horizon 2020 EU Framework Program for Research and Innovation. We thank the Helmholtz-Zentrum Berlin for the allocation of synchrotron radiation beamtime. Technical support during the measurements by Christian Weniger is acknowledged. We thank Kelly Gaffney and Philippe Wernet for fruitful discussions.

## ■ REFERENCES

- (1) Chirik, P. J. Iron- and Cobalt-Catalyzed Alkene Hydrogenation: Catalysis with Both Redox-Active and Strong Field Ligands. *Acc. Chem. Res.* **2015**, *48*, 1687–1695.
- (2) Gray, H. B.; Maverick, A. W. Solar Chemistry of Metal Complexes. *Science* **1981**, *214*, 1201–1205.
- (3) Weaver, M. J. Dynamical Solvent Effects on Activated Electron-Transfer Reactions: Principles, Pitfalls, and Progress. *Chem. Rev.* **1992**, *92*, 463–480.
- (4) Rondi, A.; Rodriguez, Y.; Feurer, T.; Cannizzo, A. Solvation-Driven Charge Transfer and Localization in Metal Complexes. *Acc. Chem. Res.* **2015**, *48*, 1432–1440.
- (5) Zhang, W.; Ji, M.; Sun, Z.; Gaffney, K. J. Dynamics of Solvent-Mediated Electron Localization in Electronically Excited Hexacyanoferrate(III). *J. Am. Chem. Soc.* **2012**, *134*, 2581–2588.
- (6) Ojeda, J.; Arrell, C. A.; Longetti, L.; Chergui, M.; Helbing, J. Charge-Transfer and Impulsive Electronic-to-Vibrational Energy Conversion in Ferricyanide: Ultrafast Photoelectron and Transient Infrared Studies. *Phys. Chem. Chem. Phys.* **2017**, *19*, 17052–17062.
- (7) Winkler, J. R.; Creutz, C.; Sutin, N. Solvent Tuning of the Excited-State Properties of (2,2'-bipyridine)tetracyanoferrate(II): Direct Observation of a Metal-to-Ligand Charge-Transfer Excited State of Iron(II). *J. Am. Chem. Soc.* **1987**, *109*, 3470–3471.
- (8) Zhang, W.; Kjær, K. S.; Alonso-Mori, R.; Bergmann, U.; Chollet, M.; Fredin, L. A.; Hadt, R. G.; Hartsock, R. W.; Harlang, T.; Kroll, T.; et al. Manipulating Charge Transfer Excited State Relaxation and Spin Crossover in Iron Coordination Complexes with Ligand Substitution. *Chem. Sci.* **2017**, *8*, 515–523.
- (9) Kjær, K. S.; Kunnus, K.; Harlang, T. C. B.; Van Driel, T. B.; Ledbetter, K.; Hartsock, R. W.; Reinhard, M. E.; Koroidov, S.; Li, L.; Laursen, M. G.; et al. Solvent Control of Charge Transfer Excited State Relaxation Pathways in  $[\text{Fe}(2,2'\text{-bipyridine})(\text{CN})_4]^{2-}$ . *Phys. Chem. Chem. Phys.* **2018**, *20*, 4238–4249.
- (10) Jones, L. H. Nature of Bonding in Metal Cyanide Complexes as Related to Intensity and Frequency of Infrared Absorption Spectra. *Inorg. Chem.* **1963**, *2*, 777–780.
- (11) Hocking, R. K.; Wasinger, E. C.; de Groot, F. M. F.; Hodgson, K. O.; Hedman, B.; Solomon, E. I. Fe L-Edge XAS Studies of  $\text{K}_4\text{Fe}(\text{CN})_6$  and  $\text{K}_3\text{Fe}(\text{CN})_6$ : A Direct Probe of Back-Bonding. *J. Am. Chem. Soc.* **2006**, *128*, 10442–10451.
- (12) Lundberg, M.; Kroll, T.; Debeer, S.; Bergmann, U.; Wilson, S. A.; Glatzel, P.; Nordlund, D.; Hedman, B.; Hodgson, K. O.; Solomon, E. I. Metal-Ligand Covalency of Iron Complexes from High-Resolution Resonant Inelastic X-ray Scattering. *J. Am. Chem. Soc.* **2013**, *135*, 17121–17134.
- (13) Kunnus, K.; Zhang, W.; Delcey, M. G.; Pinjari, R. V.; Miedema, P. S.; Schreck, S.; Quevedo, W.; Schröder, H.; Föhlisch, A.; Gaffney, K. J.; et al. Viewing the Valence Electronic Structure of Ferric and Ferrous Hexacyanide in Solution from the Fe and Cyanide Perspectives. *J. Phys. Chem. B* **2016**, *120*, 7182–7194.
- (14) Penfold, T. J.; Reinhard, M.; Rittmann-Frank, M. H.; Tavernelli, I.; Rothlisberger, U.; Milne, C. J.; Glatzel, P.; Chergui, M. X-ray Spectroscopic Study of Solvent Effects on the Ferrous and Ferric Hexacyanide Anions. *J. Phys. Chem. A* **2014**, *118*, 9411–9418.

- (15) Ross, M.; Andersen, A.; Fox, Z. W.; Zhang, Y.; Hong, K.; Lee, J.-H.; Cordones, A.; March, A. M.; Doumy, G.; Southworth, S. H.; et al. Comprehensive Experimental and Computational Spectroscopic Study of Hexacyanoferrate Complexes in Water: From Infrared to X-ray Wavelengths. *J. Phys. Chem. B* **2018**, *122*, 5075–5086.
- (16) Toma, H. E.; Takasugi, M. S. Spectroscopic Studies of Preferential and Asymmetric Solvation in Substituted Cyanoiron(II) Complexes. *J. Solution Chem.* **1983**, *12*, 547–561.
- (17) Estrin, D. a.; Baraldo, L. M.; Slep, L. D.; Barja, B. C.; Olabe, J. a.; Paglieri, L.; Corongiu, G. Theoretical and Experimental Study of Medium Effects on the Structure and Spectroscopy of the [Fe(CN)SNO]<sub>2</sub>- Ion. *Inorg. Chem.* **1996**, *35*, 3897–3903.
- (18) Jay, R. M.; Eckert, S.; Vaz da Cruz, V.; Fondell, M.; Mitzner, R.; Föhlich, A. Covalency-Driven Preservation of Local Charge Densities in a Metal-to-Ligand Charge-Transfer Excited Iron Photosensitizer. *Angew. Chem., Int. Ed.* **2019**, *58*, 10742–10746.
- (19) Stöhr, J. *NEXAFS Spectroscopy*; Springer Series in Surface Sciences; Springer: Berlin, Heidelberg, 1992; Vol. 25.
- (20) Wasinger, E. C.; de Groot, F. M. F.; Hedman, B.; Hodgson, K. O.; Solomon, E. I. L-edge X-ray Absorption Spectroscopy of Non-Heme Iron Sites: Experimental Determination of Differential Orbital Covalency. *J. Am. Chem. Soc.* **2003**, *125*, 12894–12906.
- (21) Huse, N.; Kim, T. K.; Jamula, L.; McCusker, J. K.; de Groot, F. M. F.; Schoenlein, R. W. Photo-Induced Spin-State Conversion in Solvated Transition Metal Complexes Probed via Time-Resolved Soft X-ray Spectroscopy. *J. Am. Chem. Soc.* **2010**, *132*, 6809–6816.
- (22) Bonhommeau, S.; Ottosson, N.; Pokapanich, W.; Svensson, S.; Eberhardt, W.; Björneholm, O.; Aziz, E. F. Solvent Effect of Alcohols at the L-Edge of Iron in Solution: X-ray Absorption and Multiplet Calculations. *J. Phys. Chem. B* **2008**, *112*, 12571–12574.
- (23) Hua, W.; Tian, G.; Fronzoni, G.; Li, X.; Stener, M.; Luo, Y. Fe L-Edge X-ray Absorption Spectra of Fe(II) Polypyridyl Spin Crossover Complexes from Time-Dependent Density Functional Theory. *J. Phys. Chem. A* **2013**, *117*, 14075–14085.
- (24) Huse, N.; Cho, H.; Hong, K.; Jamula, L.; de Groot, F. M. F.; Kim, T. K.; McCusker, J. K.; Schoenlein, R. W. Femtosecond Soft X-ray Spectroscopy of Solvated Transition-Metal Complexes: Deciphering the Interplay of Electronic and Structural Dynamics. *J. Phys. Chem. Lett.* **2011**, *2*, 880–884.
- (25) Cho, H.; Strader, M. L.; Hong, K.; Jamula, L.; Gullikson, E. M.; Kim, T. K.; de Groot, F. M. F.; McCusker, J. K.; Schoenlein, R. W.; Huse, N. Ligand-Field Symmetry Effects in Fe(II) Polypyridyl Compounds Probed by Transient X-ray Absorption Spectroscopy. *Faraday Discuss.* **2012**, *157*, 463.
- (26) Fondell, M.; Eckert, S.; Jay, R. M.; Weniger, C.; Quevedo, W.; Niskanen, J.; Kennedy, B.; Sorgenfrei, F.; Schick, D.; Giangrisostomi, E.; et al. Time-Resolved Soft X-ray Absorption Spectroscopy in Transmission Mode on Liquids at MHz Repetition Rates. *Struct. Dyn.* **2017**, *4*, No. 054902.
- (27) Kubin, M.; Guo, M.; Ekimova, M.; Baker, M. L.; Kroll, T.; Källman, E.; Kern, J.; Yachandra, V. K.; Yano, J.; Nibbering, E. T. J.; et al. Direct Determination of Absolute Absorption Cross Sections at the L-Edge of Dilute Mn Complexes in Solution Using a Transmission Flatjet. *Inorg. Chem.* **2018**, *57*, 5449–5462.
- (28) Zamudio-Bayer, V.; Hirsch, K.; Langenberg, A.; Niemyer, M.; Vogel, M.; Ławicki, A.; Terasaki, A.; Lau, J. T.; von Issendorff, B. Maximum Spin Polarization in Chromium Dimer Cations as Demonstrated by X-ray Magnetic Circular Dichroism Spectroscopy. *Angew. Chem., Int. Ed.* **2015**, *54*, 4498–4501.
- (29) Koroidov, S.; Hong, K.; Kjaer, K. S.; Li, L.; Kunnus, K.; Reinhard, M.; Hartsock, R. W.; Amit, D.; Eisenberg, R.; Pemmaraju, C. D.; et al. Probing the Electron Accepting Orbitals of Ni-Centered Hydrogen Evolution Catalysts with Noninnocent Ligands by Ni L-Edge and S K-Edge X-ray Absorption. *Inorg. Chem.* **2018**, *57*, 13167–13175.
- (30) Jay, R. M.; Norell, J.; Eckert, S.; Hantschmann, M.; Beyre, M.; Kennedy, B.; Quevedo, W.; Schlotter, W. F.; Dakovski, G. L.; Minitti, M. P.; et al. Disentangling Transient Charge Density and Metal-Ligand Covalency in Photoexcited Ferricyanide with Femtosecond Resonant Inelastic Soft X-ray Scattering. *J. Phys. Chem. Lett.* **2018**, *9*, 3538–3543.
- (31) Schilt, A. A. Mixed Ligand Complexes of Iron(II) and (III) with Cyanide and Aromatic Di-imines. *J. Am. Chem. Soc.* **1960**, *82*, 3000–3005.
- (32) Miedema, P. S.; Quevedo, W.; Fondell, M. The Variable Polarization Undulator Beamline UES2 SGM at BESSY II. *JLSRF* **2016**, *2*, A70.
- (33) Ekimova, M.; Quevedo, W.; Faubel, M.; Wernet, P.; Nibbering, E. T. J. A Liquid Flatjet System for Solution Phase Soft-X-ray Spectroscopy. *Struct. Dyn.* **2015**, *2*, No. 054301.
- (34) Kubin, M.; Kern, J.; Guo, M.; Källman, E.; Mitzner, R.; Yachandra, V. K.; Lundberg, M.; Yano, J.; Wernet, P. X-ray-Induced Sample Damage at the Mn L-Edge: A Case Study for Soft X-ray Spectroscopy of Transition Metal Complexes in Solution. *Phys. Chem. Chem. Phys.* **2018**, *20*, 16817–16827.
- (35) Lindahl, Abraham; Hess; van der Spoel *GROMACS 2019 Source Code*, 2018. <https://zenodo.org/record/2424363#.XvDu6GhKjIU>.
- (36) Wu, Y.; Tepper, H. L.; Voth, G. A. Flexible Simple Point-Charge Water Model with Improved Liquid-State Properties. *J. Chem. Phys.* **2006**, *124*, No. 024503.
- (37) Jorgensen, W. L.; Maxwell, D. S.; Tirado-Rives, J. Development and Testing of the OPLS All-Atom Force Field on Conformational Energetics and Properties of Organic Liquids. *J. Am. Chem. Soc.* **1996**, *118*, 11225–11236.
- (38) Åqvist, J. Ion-Water Interaction Potentials Derived from Free Energy Perturbation Simulations. *J. Phys. Chem.* **1990**, *94*, 8021–8024.
- (39) Cacelli, I.; Prampolini, G. Parametrization and Validation of Intramolecular Force Fields Derived from DFT Calculations. *J. Chem. Theory Comput.* **2007**, *3*, 1803–1817.
- (40) Becke, A. D. Density-Functional Exchange-Energy Approximation with Correct Asymptotic Behavior. *Phys. Rev. A: At., Mol., Opt. Phys.* **1988**, *38*, 3098–3100.
- (41) Becke, A. D. A New Mixing of Hartree-Fock and Local Density-Functional Theories. *J. Chem. Phys.* **1993**, *98*, 1372–1377.
- (42) Weigend, F.; Ahlrichs, R. Balanced Basis Sets of Split Valence, Triple Zeta Valence and Quadruple Zeta Valence Quality for H to Rn: Design and Assessment of Accuracy. *Phys. Chem. Chem. Phys.* **2005**, *7*, 3297–3305.
- (43) Grimme, S.; Antony, J.; Ehrlich, S.; Krieg, H. A consistent and accurate ab initio parametrization of density functional dispersion correction (DFT-D) for the 94 elements H-Pu. *J. Chem. Phys.* **2010**, *132*, 154104.
- (44) Grimme, S.; Ehrlich, S.; Goerigk, L. Effect of the damping function in dispersion corrected density functional theory. *J. Comput. Chem.* **2011**, *32*, 1456–1465.
- (45) Neese, F.; Wennmohs, F.; Hansen, A.; Becker, U. Efficient, Approximate and Parallel Hartree-Fock and Hybrid DFT Calculations. A Chain-of-Spheres-Algorithm for the Hartree-Fock Exchange. *Chem. Phys.* **2009**, *356*, 98–109.
- (46) Weigend, F. Accurate Coulomb-Fitting Basis Sets for H to Rn. *Phys. Chem. Chem. Phys.* **2006**, *8*, 1057–1065.
- (47) Neese, F. The ORCA Program System. *Wiley Interdiscip. Rev.: Comput. Mol. Sci.* **2012**, *2*, 73–78.
- (48) Aguilar, C. M.; De Almeida, W. B.; Rocha, W. R. The Electronic Spectrum of Fe<sup>2+</sup> Ion in Aqueous Solution: A Sequential Monte Carlo/Quantum Mechanical Study. *Chem. Phys. Lett.* **2007**, *449*, 144.
- (49) Price, M. L. P.; Ostrovsky, D.; Jorgensen, W. L. Gas-phase and Liquid-state Properties of Esters, Nitriles, and Nitro Compounds with the OPLS-AA Force Field. *J. Comput. Chem.* **2001**, *22*, 1340.
- (50) Prampolini, G.; Yu, P.; Pizzanelli, S.; Cacelli, I.; Yang, F.; Zhao, J.; Wang, J. Structure and Dynamics of Ferrocyanide and Ferricyanide Anions in Water and Heavy Water: An Insight by MD Simulations and 2D IR Spectroscopy. *J. Phys. Chem. B* **2014**, *118*, 14899–14912.
- (51) Breneman, C. M.; Wiberg, K. B. Determining Atom-Centered Monopoles from Molecular Electrostatic Potentials. The Need for

High Sampling Density in Formamide Conformational Analysis. *J. Comput. Chem.* **1990**, *11*, 361–373.

(52) Lu, T.; Chen, F. Multiwfn: A Multifunctional Wavefunction Analyzer. *J. Comput. Chem.* **2012**, *33*, 580–592.

(53) Barone, V.; Cossi, M. Quantum Calculation of Molecular Energies and Energy Gradients in Solution by a Conductor Solvent Model. *J. Phys. Chem. A* **1998**, *102*, 1995–2001.

(54) de Souza, B.; Farias, G.; Neese, F.; Izsák, R. Predicting Phosphorescence Rates of Light Organic Molecules Using Time-Dependent Density Functional Theory and the Path Integral Approach to Dynamics. *J. Chem. Theory Comput.* **2019**, *15*, 1896–1904.

(55) Zhao, Y.; Truhlar, D. G. The M06 Suite of Density Functionals for Main Group Thermochemistry, Thermochemical Kinetics, Noncovalent Interactions, Excited States, and Transition Elements: Two New Functionals and Systematic Testing of Four M06-Class Functionals and 12 Other Functionals. *Theor. Chem. Acc.* **2008**, *120*, 215–241.

(56) Dapprich, S.; Frenking, G. Investigation of Donor-Acceptor Interactions: A Charge Decomposition Analysis Using Fragment Molecular Orbitals. *J. Phys. Chem.* **1995**, *99*, 9352–9362.

(57) Xiao, M.; Lu, T. Generalized charge decomposition analysis (GCDA) method. *Journal of Advances in Physical Chemistry* **2015**, *4*, 111–124.

(58) Taft, R. W.; Pienta, N. J.; Kamlet, M. J.; Arnett, E. M. Linear Solvation Energy Relationships. 7. Correlations Between the Solvent-Donicity and Acceptor-Number Scales and the Solvatochromic Parameters.  $\pi^*$ ,  $\alpha$ , and  $\beta$ . *J. Org. Chem.* **1981**, *46*, 661–667.

(59) Henke, B.; Gullikson, E.; Davis, J. X-ray Interactions: Photoabsorption, Scattering, Transmission, and Reflection at  $E = 50\text{--}30,000$  eV,  $Z = 1\text{--}92$ . *At. Data Nucl. Data Tables* **1993**, *54*, 181–342.

(60) Jay, R. M.; Eckert, S.; Fondell, M.; Miedema, P. S.; Norell, J.; Pietzsch, A.; Quevedo, W.; Niskanen, J.; Kunnus, K.; Föhlisch, A. The Nature of Frontier Orbitals Under Systematic Ligand Exchange in (Pseudo-)Octahedral Fe(II) Complexes. *Phys. Chem. Chem. Phys.* **2018**, *20*, 27745–27751.

(61) Van Kuiken, B. E.; Huse, N.; Cho, H.; Strader, M. L.; Lynch, M. S.; Schoenlein, R. W.; Khalil, M. Probing the Electronic Structure of a Photoexcited Solar Cell Dye with Transient X-ray Absorption Spectroscopy. *J. Phys. Chem. Lett.* **2012**, *3*, 1695–1700.

(62) Van Kuiken, B. E.; Valiev, M.; Daifuku, S. L.; Bannan, C.; Strader, M. L.; Cho, H.; Huse, N.; Schoenlein, R. W.; Govind, N.; Khalil, M. Simulating Ru L<sub>3</sub>-Edge X-ray Absorption Spectroscopy with Time-Dependent Density Functional Theory: Model Complexes and Electron Localization in Mixed-Valence Metal Dimers. *J. Phys. Chem. A* **2013**, *117*, 4444–4454.

(63) Campbell, J.; Papp, T. Widths of the Atomic K-N<sub>7</sub> Levels. *At. Data Nucl. Data Tables* **2001**, *77*, 1–56.

(64) Hussain, A.; Huse, N.; Vendrell, O. Sensitivity of Core-Level Spectroscopy to Electrostatic Environments of Nitrile Groups: An Ab Initio Study. *Struct. Dyn.* **2017**, *4*, No. 054102.

(65) Johansson, M. P.; Blomberg, M. R.; Sundholm, D.; Wikström, M. Change in Electron and Spin Density Upon Electron Transfer to Haem. *Biochim. Biophys. Acta, Bioenerg.* **2002**, *1553*, 183–187.

(66) Kubin, M.; Guo, M.; Kroll, T.; Löchel, H.; Källman, E.; Baker, M. L.; Mitzner, R.; Gul, S.; Kern, J.; Föhlisch, A.; et al. Probing the Oxidation State of Transition Metal Complexes: A Case Study on how Charge and Spin Densities Determine Mn L-Edge X-ray Absorption Energies. *Chemical Science* **2018**, *9*, 6813–6829.

(67) Hirsch, K.; Zamudio-Bayer, V.; Rittmann, J.; Langenberg, A.; Vogel, M.; Möller, T.; Issendorff, B. v.; Lau, J. T. Initial- and Final-State Effects on Screening and Branching Ratio in X-ray Absorption of Size-Selected Free 3d Transition Metal Clusters. *Phys. Rev. B: Condens. Matter Mater. Phys.* **2012**, *86*, 165402.

(68) Godehusen, K.; Richter, T.; Zimmermann, P.; Wernet, P. Iron L-Edge Absorption Spectroscopy of Iron Pentacarbonyl and Ferrocene in the Gas Phase. *J. Phys. Chem. A* **2017**, *121*, 66–72.

(69) Roemelt, M.; Maganas, D.; DeBeer, S.; Neese, F. A combined DFT and restricted open-shell configuration interaction method including spin-orbit coupling: Application to transition metal L-edge X-ray absorption spectroscopy. *J. Chem. Phys.* **2013**, *138*, 204101.

(70) Delcey, M. G.; Sørensen, L. K.; Vacher, M.; Couto, R. C.; Lundberg, M. Efficient Calculations of a Large Number of Highly Excited States for Multiconfigurational Wavefunctions. *J. Comput. Chem.* **2019**, *40*, 1789–1799.

(71) Josefsson, I.; Kunnus, K.; Schreck, S.; Föhlisch, A.; de Groot, F.; Wernet, P.; Odelius, M. Ab Initio Calculations of X-ray Spectra: Atomic Multiplet and Molecular Orbital Effects in a Multiconfigurational SCF Approach to the L-Edge Spectra of Transition Metal Complexes. *J. Phys. Chem. Lett.* **2012**, *3*, 3565–3570.

(72) Wernet, P.; Kunnus, K.; Josefsson, I.; Rajkovic, I.; Quevedo, W.; Beye, M.; Schreck, S.; Grübel, S.; Scholz, M.; Nordlund, D.; et al. Orbital-Specific Mapping of the Ligand Exchange Dynamics of Fe(CO)<sub>5</sub> in Solution. *Nature* **2015**, *520*, 78–81.

(73) Norell, J.; Jay, R. M.; Hantschmann, M.; Eckert, S.; Guo, M.; Gaffney, K. J.; Wernet, P.; Lundberg, M.; Föhlisch, A.; Odelius, M. Fingerprints of Electronic, Spin and Structural Dynamics from Resonant Inelastic Soft X-ray Scattering in Transient Photo-Chemical Species. *Phys. Chem. Chem. Phys.* **2018**, *20*, 7243–7253.